OPEN ACCESS

Heavy charged particles in radiation biology and biophysics

New Journal of Physics
The open-access journal for physics

Heavy charged particles in radiation biology and biophysics

H Nikjoo[1,5], S Uehara[2], D Emfietzoglou[3] and A Brahme[4]

[1] Radiation Biophysics, Medical Radiation Physics Department, Karolinska Institute, Box 260, SE-171 76 Stockholm, Sweden
[2] School of Health Sciences, Kyushu University, Fukuoka, Japan
[3] Medical Physics Laboratory, University of Ioannina Medical School, 451 10 Ioannina, Greece
[4] Medical Radiation Physics, Karolinska Institute, Stockholm, Sweden
E-mail: hooshang.nikjoo@ki.se

New Journal of Physics **10** (2008) 075006 (28pp)
Received 5 February 2008
Published 28 July 2008
Online at http://www.njp.org/
doi:10.1088/1367-2630/10/7/075006

Abstract. Ionizing radiations induce a variety of molecular and cellular types of damage in mammalian cells as a result of energy deposition by the radiation track. In general, tracks are divided into two classes of sparsely ionizing ones such as electron tracks and densely ionizing tracks such as heavy ions. The paper discusses various aspects and differences between the two types of radiations and their efficacies in radiation therapy. Biophysical studies of radiation tracks have provided much of the insight in mechanistic understanding of the relationship between the initial physical events and observed biological responses. Therefore, development of Monte Carlo track-structure techniques and codes are paramount for the progress of the field. In this paper, we report for the first time the latest development for the simulation of proton tracks up to 200 MeV similar to beam energies in proton radiotherapy and space radiation. Vital to the development of the models for ion tracks is the accurate simulation of electron tracks cross sections in liquid water. In this paper, we report the development of electron track cross sections in liquid water using a new dielectric model of low-energy electrons accurate to nearly 10% down to 100 eV.

[5] Author to whom any correspondence should be addressed.

Contents

1. Introduction

The relationship between the quality of ionizing radiation and cell response has been the subject of much debate over the past half century. In this paper, we discuss a few selected aspects of biological significance and relative importance of heavy ions of low atomic number (z) versus electrons. In the context of biophysics, we present development of two new tools for simulation of energetic protons from 1 keV–200 MeV and a new significant breakthrough in modelling of electron track structure in liquid water as a surrogate for tissue. In the context of radiotherapy, we discuss the merits of therapy with heavy ions. It is noteworthy to state, by definition, by heavy ions we mean protons and ions of higher z values.

Two major achievements in the 20th century were mapping of the human genome and human space exploration. In the former, we seek to understand the underlying genetics of human disease, in particular cancer, and to create new therapy regimes and drug delivery systems. In space research, we seek to understand and overcome many of the human frailties for long-term space travel and seek biomedical and technological advances to reduce the risks. In both the scenarios, ionizing radiation acts like a double-edged sword. In one, we have used radiation as a curing agent and in the other, it is a major carcinogenic agent limiting the scope and duration of deep space human exploration. In this paper, by definition, the term heavy ion refers to protons and higher atomic number ions. Considerable resources have been utilized either to mitigate the risk associated with the exposure or devise methods with more efficient delivery of the radiation beam to eradicate the tumour. In parallel with these activities, understanding the mechanism of radiation action in human cells and tissue has been an ongoing process since the discovery of x-rays. Scientific interest in understanding the mechanism of radiation action was generally formalized with the publication of the book by Douglas Lea in 1947 and the birth of radiobiology. Since then, many fundamental questions have been elucidated, many more

remain. What is the target for radiation—is it a single cell or a tissue? Is the response, dose-, dose-rate- and particle-dependent? Are observed biological lesions a function of physical properties of the radiation track or entirely dictated by physiological, biological and genetic responses to damaged cell and tissue? Is there a lower level threshold to radiation response? Ionizing radiation causes DNA damage and may lead to chromosome damage, mutation and cell transformation. What is the risk from exposures to chronic and acute radiation? Is cancer a chromosomal or mutational disease? How safe is radiation therapy using photons versus protons, carbon and other heavy ions? These are a few questions, but there remain many more on the role of genetic instability and bystander effects. For example, to date, 291 cancer genes have been discovered (1% of all genes, http://www.sanger.ac.uk). There have been more than 241 000 experiments on the causes of cancer, more than 1800 experiments on various tumours, $>24\,000$ experiments on somatic mutations and greater than 3200 experiments on involvement of various genes in different cancers. Despite such efforts there still remains a gap in understanding observed biological lesions, chromosomal aberrations, mutations and cell transformations, with cancer induction.

In line with the experimental approach to radiobiological problems, theoretical and modelling approaches have played a significant role in the development of mechanistic models in radiobiology to guide experiments. Biophysical models have provided useful predictions on biological phenomena, for example the role of kinase pathways in human diseases, differences between the low and the high linear energy transfer (LET) radiations and predictions on the frequencies of the spectrum of DNA damage. In general, theoretical and computational approaches are known as *microdosimetry* and *radiation biophysics*. The principle aim of radiation biophysics is to characterize the primary properties of the radiation track which determines the effect of radiation in mammalian cells and tissue. The theoretical approach then tries to relate the physical properties to the observed biological responses to radiations of different qualities and their implications in radiation therapy and radiation protection.

2. General features of cell response to ionizing radiation

Interaction of ionizing radiation with mammalian cells induces a variety of damage in DNA as the result of energy deposition in the cell nucleus [1]. DNA damage could lead to senescence, necrosis and apoptosis, mutation, chromosome damage, mitotic catastrophe, genetic instability and most importantly to a fully repaired surviving cell. Damage to the cell or the consequence of the damage can also cause release of certain cytokines which could affect neighbouring cells. The latter process is known as the bystander effect [2, 3]. The process of energy deposition starts with ionizations and excitations of DNA and the surroundings. For example, a 1 Gy irradiation of the cell with low and high LET could cause, on average, a large number of events. But not every physical or chemical event in the form of ionization and excitation, hydrated electrons and other molecular products leads to recognizable molecular damage in the form of strand breakage and base damage. In principle, there is no simple relationship between the DNA damage and cell survival. Assuming a single hit mechanism and Poisson statistics, the 37% survival level corresponds on average to one lethal hit per cell. This value is cell type and cell-cycle dependent. For mammalian cell lines, it varies between 20 and 80 double strand breaks (DSB) per lethal event, for HF19, a more sensitive tumour cell line, it is about 20. A popular hypothesis in the field is the concept of clustered DNA damage. The hypothesis puts forward the concept that the more complex the DNA damage, the more difficult it is to

repair it, thereby causing more lethality. Therefore, a greater percentage of cells exposed to low LET irradiation survive, because they are repaired more readily than those exposed to high LET radiation, as the latter produces more complex forms of DNA damage per unit dose absorbed and per genome. Experiments and model calculations show that the relative biological effectiveness for induction of double-strand breaks as a function of the LET of the particle is unity for all radiations [4]–[9]. Modelling and calculations of frequencies of the spectrum of DNA damage has been carried out by a number of authors [10]–[12]. Monte Carlo modelling of the yield of initial complex double-strand breaks increases with the LET of the radiation up to a few hundred kilo-electron-volts per micrometre [6, 10]. Experimental work to confirm such findings supports the model and calculations that complexity of DNA damage may be a very important parameter in repair and survival [13]–[16].

3. Frequencies of energy deposition by heavy ions

The central parameter of radiation dosimetry is the absorbed dose in the volume of the target. Absorbed dose defined as the quotient of the local energy deposited in the volume of interest by the radiation track(s) and the mass of the volume. In line with this, the differences in quality of radiations in terms of spatial and temporal distributions of radiation interactions in the volume of interest can be obtained as the absolute frequency of energy deposition. Such data in particular for protons and heavier ions is a rich source of data for biophysical analysis. Such differences can only become meaningful when the dimensions of target volumes become sufficiently small, 1–100 nm diameter of a sphere or a cylinder. Spheres and cylinders, in general, mimic most biological targets such as cells and linear segments of DNA or its macromolecular structures. By energy-deposition events we mean inelastic events such as ionizations and excitations. Figure 1 presents an example of absolute frequencies of energy depositions in a segment of chromatin fibre, 30 nm diameter by 30 nm length cylinders, for selected energies of protons, α-particles, carbon and iron ions. The abscissa is the energy deposited or greater in the target volume in electron volts and the ordinate gives the absolute frequency of energy depositions per Gy per target. A number of monographs of frequencies of energy depositions for target sizes 1–100 nm and aspect ratios 0.5–8 for electrons (10 eV–100 keV) [17], ultrasoft x-rays (278 eV C, 1.5 keV Al, 4.5 keV Ti and 8 keV Cu) [18], protons (1–26 keV) [19], protons and alpha-particles (0.3–4 MeV u^{-1}) [20], alpha-particles (1 keV u^{-1}–2 MeV u^{-1}) [21] and low-energy heavy ions (H, Li, Be, C and O) [22] have been published. A complete set of microdosimetry parameters can be derived from these distributions [23].

4. The clinical efficiency of heavy ions

The major problem with classical low LET radiation therapy using electrons and photons is the presence of hypoxic and otherwise radiation-resistant tumours, where the dose to the tumour cannot be sufficiently increased without severely damaging the surrounding normal tissues. During the last 15 years, the treatment results have been improved substantially by using physically optimized intensity-modulated photon therapy (IMRT) and to some extent also proton therapy with 3D spot scanning to maximize the tumour dose and minimize the side effects in normal tissues. Further improvements can be achieved using low LET radiations by more accurate determination of the optimal dose delivery based on radiobiological treatment objectives such as maximizing the probability of achieving complication-free tumour cure. To

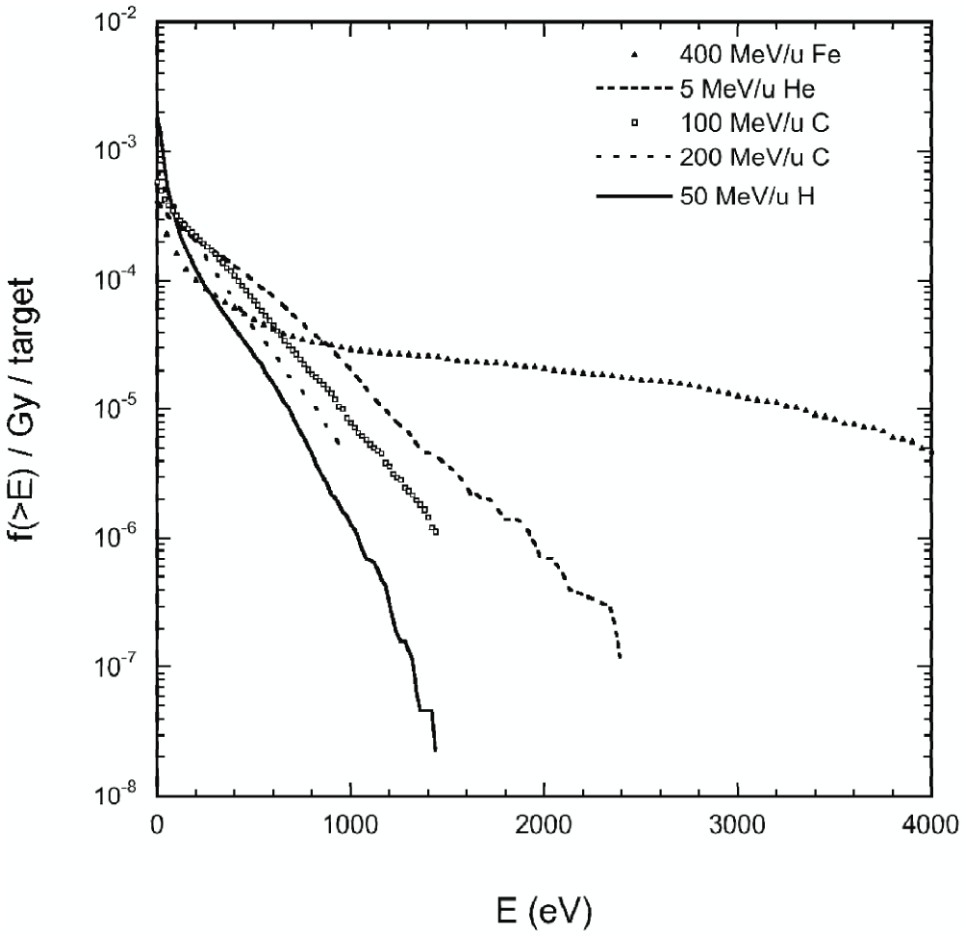

Figure 1. Frequency distributions of energy deposition in a target volume corresponding approximately to a segment of chromatin fibre 30 nm in length and 30 nm in diameter, in water, irradiated with alpha-particles, protons and iron ions. The ordinate gives the absolute frequency ($f > E$) of deposition events greater than the energy E (eV) in the target when randomly placed in water uniformly irradiated with 1 Gy of the given radiation.

get further with severely hypoxic tumours, such as lung tumours, prostate cancer and bone- and soft-tissue sarcoma, a higher therapeutic effect on the gross tumour growth is essential [24]. This can be achieved using ions heavier than protons and to some extent with ions beyond carbon. However, an increased ionization density on its own is not sufficient to increase the treatment outcome as was seen with neutron therapy. The increased LET of neutrons and ions heavier than protons will certainly increase the cell kill in the tumour. But exposure of normal tissue to a high LET radiation is a major disadvantage as the cellular damage will be largely irreparable and the healthy tissue will not recover overnight as it largely does with low LET radiation damage.

The optimal radiation modality for radiation therapy should therefore have the highest possible LET in the Bragg peak and be primarily placed in the tumour area and mainly have a low LET component in the entrance and plateau regions, which essentially passes through shallow normal tissues. And the same should preferably be the case in the fragmentation tail

Table 1. Biochemical relapse-free survival at 5 years for photon (conformal and IMRT), proton and carbon ion therapy of prostate cancer.

PSA subgroup	Photon Memorial 2005[a]			Proton Loma Linda 2004[b]		Carbon NIRS 2004[c]	
	Survival 3D conformal (%)	Number of patients IMRT	Survival IMRT (%)	Number of patients	Survival (%)	Number of patients	Survival (%)
<4.1 ng/ml	77	403	90	106	90	3	100
4.1–10				606	84	60	92
10.1–20.0	50	476	70	339	65	73	88
20.1–	21	292	48	133	45	112	87

[a]Zelefsky [26].
[b]Slater *et al* [27].
[c]Tsujii [28].

beyond the Bragg peak since this too often reaches intact normal tissues. From this point of view, ions from helium to carbon are most interesting, since protons are essentially low LET-type, whereas heavier ions beyond carbon contain increasingly high LET-type in the plateau region and fragmentation tail. In fact, as was shown recently, the most ideal ion for small tumours is probably lithium ions since they have low LET component in practically the entire plateau and a small fragmentation tail region [25]. For the largest tumours, carbon and oxygen ions may even be of interest since the high-LET region can reach as far as 4–6 cm in front of and behind the Bragg peak. However, if radiation-sensitive normal tissues of essentially parallel intrinsic organization, such as the spinal cord are located close to the tumour, it is essential that no irradiation from the Bragg peaks or the high LET component falls there to avoid paralysis.

To illustrate the improvement in clinical efficiency by the abovementioned developments, some recent phase-1 and -2 clinical trial data for hundreds of prostate cancer patients are summarized in table 1. It is seen that for generally large prostate cancers with a prostate-specific antigen (PSA) level of more than 20 ng ml^{-1}, the probability for biochemical local control at 5 years was about 21% with classical conformal radiation therapy. The results more than doubled to 48% by introducing physically optimized IMRT as shown by Zelewski and co-workers at Memorial Sloan-Kettering Cancer Center in New York. With protons, the group at Loma Linda reached a similar level (45%) as expected since protons mainly have a low LET (RBE $\sim$ 1.10–1.15). However, as these prostate tumours are largely hypoxic, a significant further improvement was seen with carbon ions at the National Institute of Radiological Sciences, NIRS, in Japan with an 87% local relapse-free control at 5 years. This is almost a second doubling over the result of conformal and IMRT and proton treatments. For the smaller tumours (PSA $<$ 20) hypoxic and low LET radiation resistance is a minor problem making the difference between the four treatment techniques less pronounced. These and many similar results indicate a breakthrough in clinical outcome for advanced cancers that are difficult to cure with normal low LET radiation therapy.

Recently, it has been shown that these highly improved outcomes may partly be caused by increased probability for apoptotic cell-kill due to medium LET particles ($\sim$50 keV μm^{-1}) [29],

which have a large probability to eliminate even severely hypoxic tumour cells. About half of all the tumours were mutated in the tumour suppressor gene p53 often called 'the guardian of the genome'. In the tumours where it is intact, low LET damage often induces serine 10 and 15 phosphorylation leading to cell-cycle arrest and DNA-damage repair through p21 and GADD45 (growth arrest DNA damage) signalling [29, 30]. With low z ions this largely happens in the normal tissues, whereas in the tumour the ionization density is much higher due to the high LET Bragg peak damage that more effectively phosphorylate the serine 46 site. In the latter case, p53 selects the apoptotic (programmed cell death) pathway since this damage is more severe and difficult to repair. In tumours where p53 is mutated there are a number of other apoptotic pathways that are active at high LET and much less so at low LET, such as the ceramide pathway, which will be induced by severe membrane damage at high LET. Interestingly, the p53-dependent response is highest at medium LET; there are many more tracks through the cell nuclei per unit dose delivered [25, 29]. For many small- to medium-sized tumours, for example in paediatric tumours, the optimal radiation modality should thus be lithium to beryllium ions and as far as possible Bragg peaks reaching normal tissues outside the tumour should be avoided at all costs. The promising results from NIRS with carbon ions on larger tumours are very encouraging and point to an increased future use of ions with low z, particularly for prostate, lung, liver, head and neck cancers as well as bone- and soft-tissue sarcoma. Therefore, it is of great importance to understand better the physical and biological properties of ions with low z including proton to carbon.

The shape of the biologically effective dose-delivery with a hypoxic tumour between 10 and 15 cm is shown in figure 2 indicating that the effective dose is substantially reduced in the hypoxic volume both with photons and protons. The carbon ions have a smaller reduction due to an oxygen enhancement ratio (OER) of around 1.5 instead of 2–2.5 for photons and protons. Figure 3 shows the three field techniques used at NIRS for prostate cancer. It is interesting that a smaller number of beams are sufficient with ions due to the sharp dose-distribution—often 4–6 beams are needed with photons. Together these four examples explain the positive development going from photons to protons and to carbon ions. Therefore, it is important to understand better the optimal use of available ions for radiation therapy.

5. Cross sections for high-energy protons 1–200 MeV

In the preceding sections, we described the importance of protons and heavier ions in radiation therapy and in space travel and reasoned the need for a better understanding of their biophysical and biological aspects of their tracks. To progress on this front, a necessary tool is required to simulate tracks of ions at the molecular level. In this section we describe, for the first time, simulation of energetic protons between 1 and 200 MeV similar to protons in space and radiotherapy beams. Simulation of proton tracks is obtained for full slowing down of protons including consideration of charge exchange at energies below the Bragg peak. The cross-sections for the Monte Carlo simulation of proton tracks for low-energy protons between 1 keV and 1 MeV have been published in a previous paper [31]. The contribution of the charge transfer processes can be neglected at energies above 1 MeV. Therefore, relevant cross-sections are limited to those for ionization, excitation and elastic scattering for the projectile H^+.

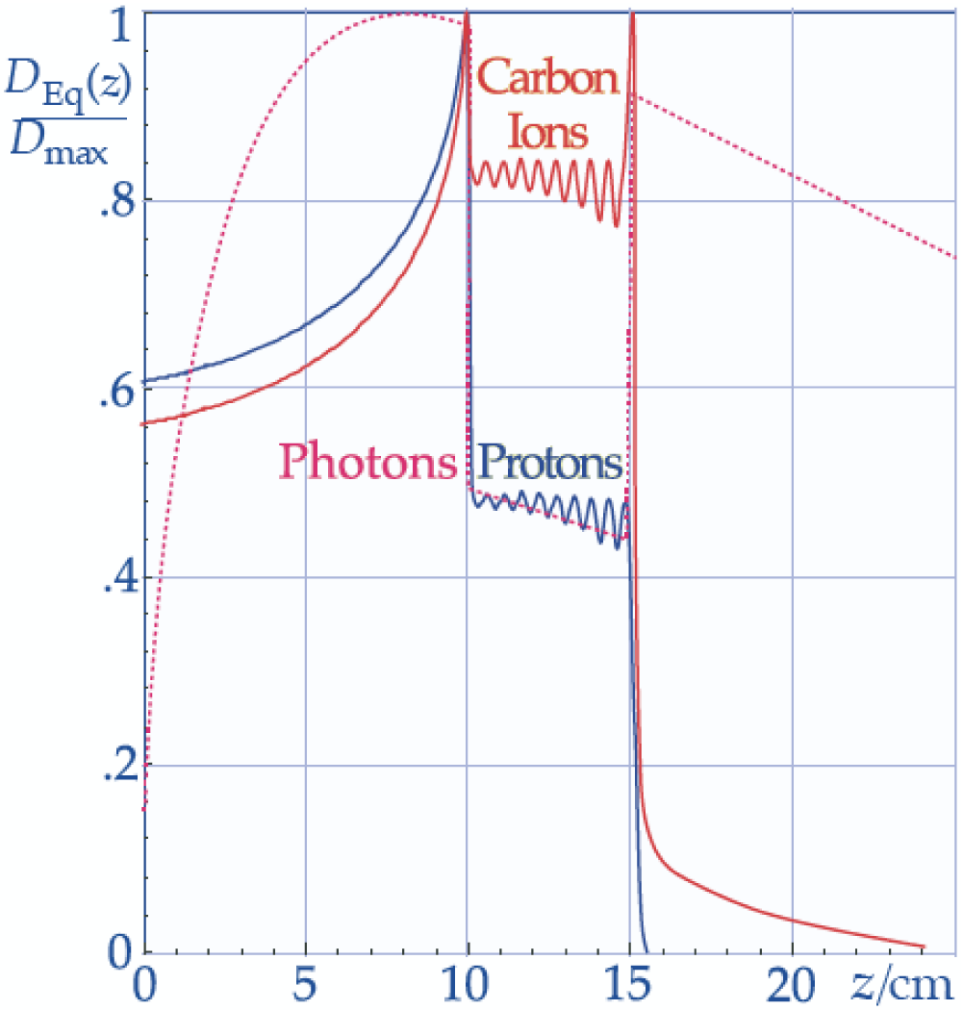

Figure 2. The biologically effective dose with a highly hypoxic tumour at a depth of 10–15 cm. Due to the large OER for photons and protons the effective dose is only 40–50% with low LET radiations, whereas for high LET carbon ions the reduction is generally much less (70–80%). This partly explains the higher efficiency of carbon ions for hypoxic prostate cancer (cf table 1).

5.1. Ionization

5.1.1. Total ionization cross sections (TICSs). TICSs for high-energy protons were obtained by energy scaling of the electron ionization cross sections. The relationship between the kinetic energy of a proton T_p and that of an electron T_e with the same speed v is given by

$$T_p = \frac{1}{2} m_p v^2 = \lambda T_e, \tag{1}$$

where λ is the mass ratio $m_p/m_e = 1836$. For example, the electron kinetic energy of 109 keV corresponds to the proton kinetic energy of 200 MeV. The proton cross-section at T_p was obtained by such scaling of the electron cross section at T_e. Therefore, we explain the formula for electron cross sections used in our electron track code KURBUC [32].

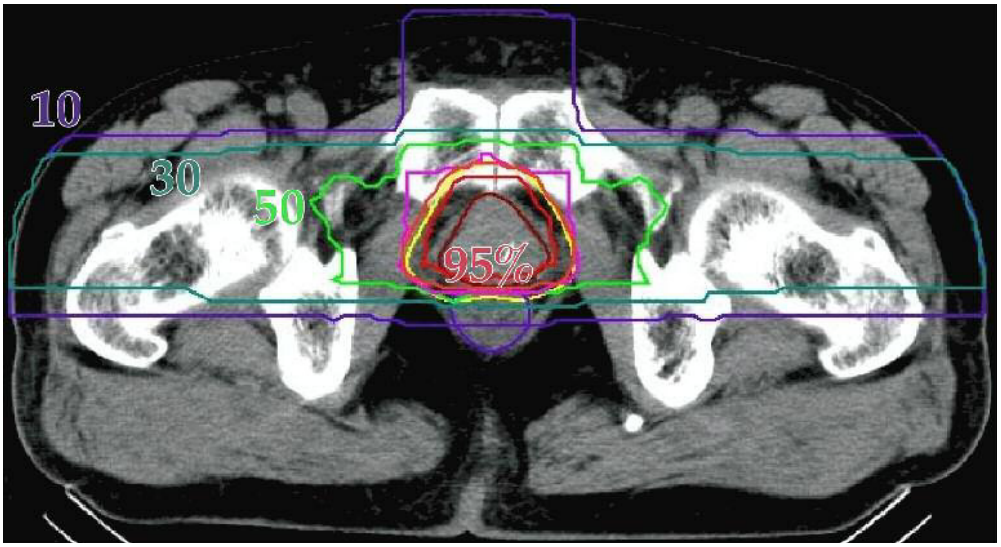

Figure 3. A typical isodose distribution for a 3-field carbon ion prostate treatment at NIRS in Japan. Twenty fractions over four weeks are delivered with a total photon-equivalent dose of 66 Gy Eq. The low dose to normal tissues surrounding the tumour is clearly seen. The increased therapeutic effect in hypoxic tumour cells is shown more clearly in figure 2.

The calculation of electron ionization cross sections was carried out using Seltzer's formula [33]. For the jth orbital of a water molecule, the cross-section differential in kinetic energy ε of the ejected electron is written as the sum of two contributions: the close collision and the distant collision

$$\frac{\mathrm{d}\sigma^{(j)}}{\mathrm{d}\varepsilon} = \frac{\mathrm{d}\sigma_{\mathrm{c}}^{(j)}}{\mathrm{d}\varepsilon} + \frac{\mathrm{d}\sigma_{\mathrm{d}}^{(j)}}{\mathrm{d}\varepsilon}. \tag{2}$$

The first term is described in terms of a collision between two electrons

$$\frac{\mathrm{d}\sigma_{\mathrm{c}}^{(j)}}{\mathrm{d}\varepsilon} = \frac{2\pi r_{\mathrm{e}}^2 m_{\mathrm{e}} c^2 n_j}{\beta^2} \frac{T}{T + B_j + U_j} \times \left\{ \frac{1}{E^2} + \frac{1}{(T-\varepsilon)^2} + \frac{1}{T^2}\left(\frac{\tau}{\tau+1}\right)^2 - \frac{1}{E(T-\varepsilon)} \frac{2\tau+1}{(\tau+1)^2} + G_j \right\}, \tag{3}$$

$$G_j = \frac{8U_j}{3\pi}\left[\frac{1}{E^3} + \frac{1}{(T-\varepsilon)^3}\right]\left[\tan^{-1}\sqrt{y} + \frac{\sqrt{y}(y-1)}{(y+1)^2}\right], \tag{4}$$

in which $r_{\mathrm{e}} = 2.81794 \times 10^{-13}$ cm, $m_{\mathrm{e}}c^2 = 511\,003.4$ eV is the electron rest mass, $\tau = T/m_{\mathrm{e}}c^2$ the kinetic energy in units of the rest mass, $\beta^2 = 1 - 1/(\tau+1)^2$, n_j the number of electrons in the orbital, B_j the orbital binding energy, U_j the mean kinetic energy of the target electron in the orbital, E the energy transfer ($= \varepsilon + B_j$) and $y = \varepsilon/U_j$.

The second term is described in terms of the interaction of the equivalent radiation field with the orbital electrons

$$\frac{\mathrm{d}\sigma_{\mathrm{d}}^{(j)}}{\mathrm{d}\varepsilon} = n_j I(E)\sigma_{\mathrm{PE}}^{(j)}(E), \tag{5}$$

where $\sigma_{\mathrm{PE}}^{(j)}$ is the photoelectric cross section for the jth orbital (per orbital electron), for an incident photon of energy $E = \varepsilon + B_j$. The virtual-photon spectrum integrated over impact parameters $b_{\min} < b < b_{\max}$ is given by

$$I(E) = \frac{2}{137\pi\beta^2 E}[G(x_{\min}) - H(x_{\max})],$$

$$G(x_{\min}) = x_{\min}K_0(x_{\min})K_1(x_{\min}) - \frac{x_{\min}^2}{2}\left\{K_1^2(x_{\min}) - K_0^2(x_{\min})\right\}, \tag{6}$$

$$H(x_{\max}) = x_{\max}K_0(x_{\max})K_1(x_{\max}) - \frac{x_{\max}^2}{2}\left\{K_1^2(x_{\max}) - K_0^2(x_{\max})\right\},$$

where

$$x_{\min} = \frac{Eb_{\min}}{\hbar c}\frac{\sqrt{1-\beta^2}}{\beta}, \tag{7}$$

$$x_{\max} = \frac{Eb_{\max}}{\hbar c}\frac{\sqrt{1-\beta^2}}{\beta}, \tag{8}$$

$b_{\min}$ and $b_{\max}$ are impact parameters. $b_{\min} = \langle r \rangle_j$ is the expectation value of the electron radius for the orbital of interest and $b_{\max}$ is given by

$$b_{\max} = \frac{1.123\hbar c\beta}{B_j\sqrt{1-\beta^2}}, \tag{9}$$

where K_0 and K_1 are the Bessel functions of the order of 0 and 1. It should also be noted that $I(E)$, $x_{\min}$ and $b_{\min}$ are different for each orbital.

The partial ionization cross-section for a molecular orbital is given by

$$\sigma^{(j)} = \int_0^{(T-B_j)/2} \frac{\mathrm{d}\sigma^{(j)}}{\mathrm{d}\varepsilon}\,\mathrm{d}\varepsilon. \tag{10}$$

The TICS is given by

$$\sigma_{\mathrm{ion}} = \sum_{j=1}^{5} \sigma^{(j)}. \tag{11}$$

Various input data requisite for numerical calculations for a water molecule were taken from the published literature. These include atomic data for each shell of hydrogen and oxygen, the atomic electron radii $\langle r \rangle$ and the molecular radii $\langle r \rangle_j$, the photoelectric cross-sections $\sigma_{\mathrm{PE}}^{(j)}$ for molecular orbitals, values of B_j and U_j of the orbital electron, and so on. Detailed descriptions and the data are given in the previous paper [32]. Partial and total ionization cross sections were calculated from 10 eV to the mega-electron-volt region. Both the cross sections for the energy range of electrons between 545 eV and 109 keV were used for cross sections for the corresponding proton energy range between 1 and 200 MeV. A minor adjustment was made for the energies higher than 150 MeV in order to reproduce the proper continuous slowing-down ranges and the stopping powers. Figure 4 shows the TICSs including those for energies lower than 1 MeV.

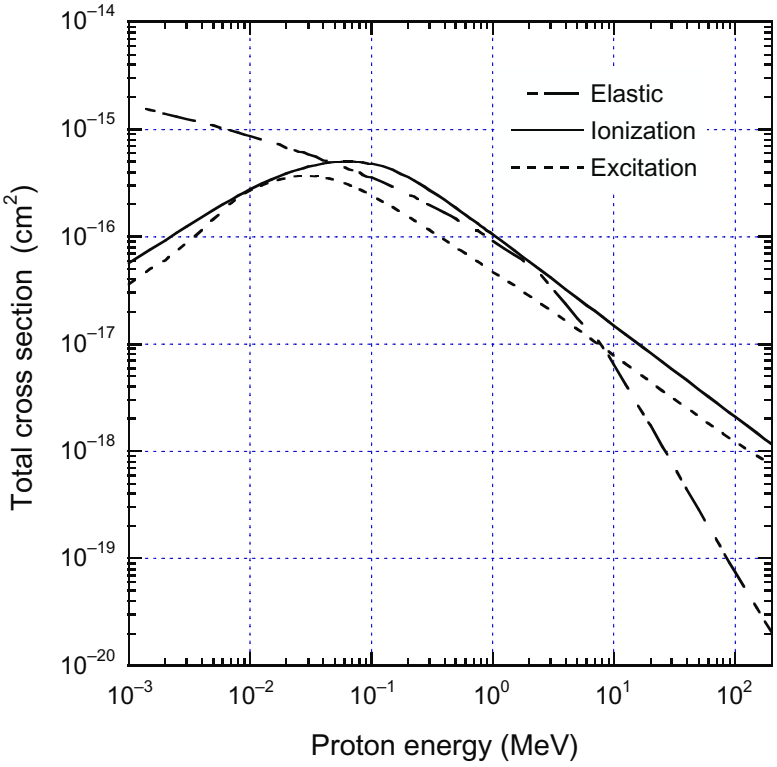

Figure 4. Total cross-sections due to proton impact on water. Those for energies lower than 1 MeV were the same as the previous paper [31]. TICS for high-energy protons were obtained by energy scaling of the electron ionization cross sections as described in section 5.1.1. Excitation cross sections were calculated using equation (15). Elastic scattering cross sections were calculated using equation (26).

5.1.2. Single differential cross sections (SDCSs). The collision of a charged particle with another at rest is described by the Rutherford scattering formula [34]

$$\frac{\mathrm{d}\sigma_{\mathrm{R}}}{\mathrm{d}\varepsilon} = \frac{4\pi a_0^2}{T}\left(\frac{R}{E}\right)^2, \tag{12}$$

where ε is the kinetic energy of the secondary electron after the collision, T the kinetic energy of an electron with the same speed as the incident proton, i.e. $T = T_{\mathrm{p}}/\lambda$, a_0 the Bohr radius, R the Rydberg energy (13.6 eV), and $E = \varepsilon + B$ the energy transfer in which B is the binding energy of a molecular orbital.

Based on the Rutherford formula, the binary-encounter approximation treats the collision as a classical one between the projectile and a single electron in the target. A simpler form of the binary-encounter theory leads to a singly differential cross section of the form [34]

$$\frac{\mathrm{d}\sigma_{\mathrm{BE}}}{\mathrm{d}\varepsilon} = \left(\frac{\mathrm{d}\sigma_{\mathrm{R}}}{\mathrm{d}\varepsilon}\right)\left(1+\frac{4U}{3E}\right), \quad \text{for } E_{\min} \leqslant E \leqslant E_-, \tag{13a}$$

$$\frac{\mathrm{d}\sigma_{\mathrm{BE}}}{\mathrm{d}\varepsilon} = \left(\frac{\mathrm{d}\sigma_{\mathrm{R}}}{\mathrm{d}\varepsilon}\right)\left(\frac{U}{6E}\right)\left\{\left(\frac{4T}{U}\right)^{3/2} + \left[1-\sqrt{1+\frac{E}{U}}\right]^3\right\} \quad \text{for } E_- \leqslant E \leqslant E_+, \tag{13b}$$

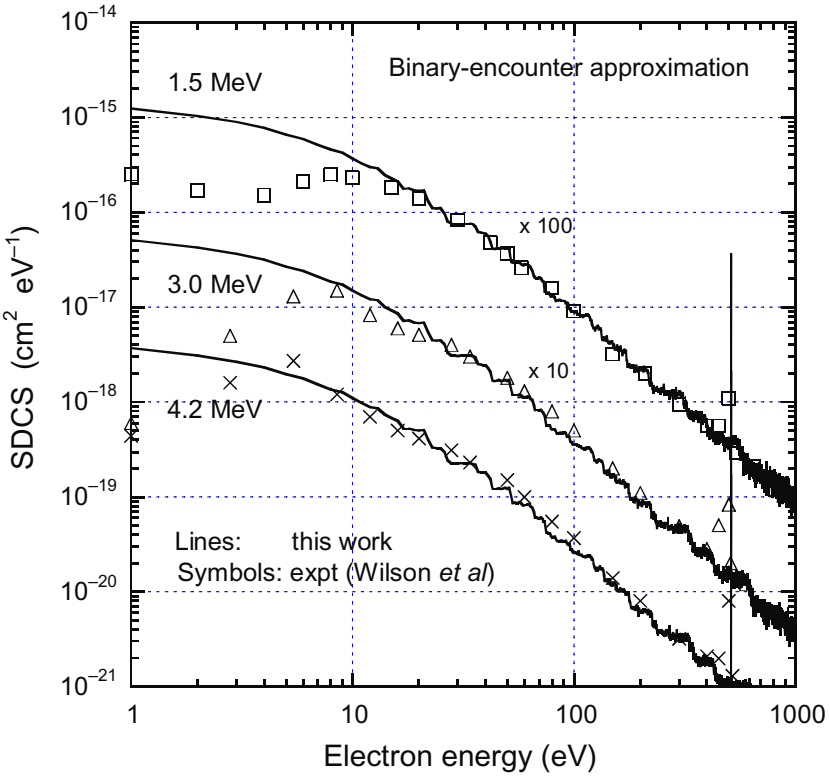

Figure 5. Randomly sampled energy spectra for secondary electrons ejected by proton impact in comparison with the experimental data taken from Wilson *et al* [35].

and

$$\frac{\mathrm{d}\sigma_{\mathrm{BE}}}{\mathrm{d}\varepsilon} = 0, \quad \text{for } E > E_+, \tag{13c}$$

where U is the kinetic energy of the target electron and

$$E_\pm = 4T \pm 4(TU)^{1/2}. \tag{13d}$$

Figure 5 shows the randomly sampled energy spectra of secondary electrons for the proton energies 1.5, 3 and 4.2 MeV in comparison with the experimental data by Wilson *et al* [35]. The sampled spectra were scaled to fit to the absolute experimental data.

5.1.3. Angular distributions for secondary electrons. For low-energy proton impact, experimental angular distributions of electrons ejected from water by proton impact were used. Experimental data are unavailable for high-energy protons >1 MeV. The initial emission angle for secondary electrons was approximated by the kinematical relationship:

$$\cos\theta = \sqrt{\frac{\lambda\varepsilon}{4T_{\mathrm{p}}}}. \tag{14}$$

This equation suggests almost all of the secondary electrons are ejected vertically from the projectile path. The tracks of secondary electrons were generated by the electron code KURBUC which is effective for the electron energy of 10 MeV.

5.2. Excitation

Excitation cross sections and mean excitation energy loss by proton impact on water molecules were treated based on the formula given by Miller and Green [36]. The formula was used for the low-energy protons [31]. They assumed an analytical function for each excited level of the form

$$\sigma_{\mathrm{exc}}(T) = \frac{\sigma_0 (Za)^{\Omega} (T - W)^{\nu}}{I^{\Omega+\nu} + T^{\Omega+\nu}}, \tag{15}$$

where $\sigma_0 = 10^{-16}\,\mathrm{cm}^2$ and $Z = 10$; W, a, I, Ω and ν for 28 excitation states are given in table III of [36]. The calculated total cross sections are shown in figure 4. They noted that their excitation cross sections were only rough estimates proposed in the absence of detailed theoretical or experimental data. They further noted that the position and height of the maximum in the cross section could easily be in error by a factor of two.

The mean excitation energy W_{av} was calculated using the relationship $\Sigma W_j \sigma_{\mathrm{e}j}(T)/\Sigma\sigma_{\mathrm{e}j}(T)$, where W_j is the excitation threshold energy and $\sigma_{\mathrm{e}j}(T)$ is the excitation cross section of equation (15) above for state j.

5.3. Elastic scattering

5.3.1. Total cross sections. The classical mechanics trajectory calculations (CMTCs) were applied to the calculations of total elastic cross sections for high-energy protons. This method is just the same as for the previous work on low-energy protons lower than 1 MeV [31]. The interaction between the projectile and the target atom can be described in terms of a potential function

$$V(r) = (zZe^2/r) F_{\mathrm{s}}(r/r_{\mathrm{s}}). \tag{16}$$

The first factor in equation (16) is the Coulomb potential for two bare nuclei with charges ze and Ze. The factor $F_{\mathrm{s}}(r/r_{\mathrm{s}})$ takes into account the screening by atomic electrons. The extent of screening is characterized by the screening length, r_{s}. A commonly used prescription for the screening length is

$$r_{\mathrm{s}} = 0.88534 r_{\mathrm{B}} (z^{2/3} + Z^{2/3})^{-1/2}, \tag{17}$$

where r_{B} is the Bohr radius and 0.88534 is a numerical constant from the Thomas–Fermi model of the atom. For protons, a screening function $F_{\mathrm{s}}(r/r_{\mathrm{s}})$ is given by the International Commission of Radiation Units (ICRU) [37]

$$F_{\mathrm{s}}(r/r_{\mathrm{s}}) = 0.10\mathrm{e}^{-6r/r_{\mathrm{s}}} + 0.55\mathrm{e}^{-1.2r/r_{\mathrm{s}}} + 0.35\mathrm{e}^{-0.3r/r_{\mathrm{s}}}. \tag{18}$$

For a particle scattered in a central potential $V(r)$, the deflection angle θ is obtained in a CMTC as a function of the impact parameter, p [37]

$$\theta = \pi - 2\int_{r_{\mathrm{min}}}^{\infty} \frac{p}{r^2\sqrt{1 - V(r)/T_{\mathrm{cm}} - p^2/r^2}}\,\mathrm{d}r, \tag{19}$$

where r_{min} is the distance of the closest approach. This value is given by the positive root of the following:

$$r^2 - 2zZr_{\mathrm{e}}\frac{m_{\mathrm{e}}c^2}{\beta Pc} r F_{\mathrm{s}}(r/r_{\mathrm{s}}) - p^2 = 0, \tag{20}$$

in which

$$\beta = \sqrt{1 - \left(\frac{m_p c^2}{T + m_p c^2}\right)^2}, \qquad Pc = \sqrt{(T + m_p c^2)^2 - (m_p c^2)^2}, \tag{21}$$

$m_p c^2$ = proton rest mass, and P is the momentum of the proton. T_{cm} is the particle energy in the centre-of-mass system, given by

$$T_{cm} = \frac{T}{1 + m_p / M_t}, \tag{22}$$

where T is the kinetic energy in the laboratory system, and m_p and M_t are the masses of the proton and target atom. Equation (19) was solved numerically using procedures given by Everhart *et al* [38] and Wilson and Haggmark [39]. Thereby the deflection angle θ was obtained as a function of the impact parameter p. The boundary of 'large-angle calculations' and 'small-angle calculations' described by Everhart *et al* was set at $\theta = 0.1\pi$, where smooth transitions are given.

The differential elastic scattering cross section can be obtained by numerical differentiation of the curve of impact parameter versus deflection angle using a B-spline interpolation

$$\frac{d\sigma_{el}}{d\Omega} = -\frac{p}{\sin\theta}\frac{dp}{d\theta}, \tag{23}$$

where θ and $d\sigma_{el}/d\Omega$ are functions of the impact parameter and the particle energy. The energy deposition ΔE in elastic scattering depends on both the scattering angle and the proton energy. This is given by the formula $W(\theta, T)$ according to ICRU 49 [37]

$$\Delta E = W(\theta, T) = 4T\frac{m_p M_t}{(m_p + M_t)^2}\sin^2\frac{\theta}{2}. \tag{24}$$

In order to reduce the divergence of the total cross section, the cut-off angles, θ_{cut}, were set such as to limit the increase in the scattering probability at low scattering angles [40].

$$\theta_{cut} \approx \frac{1}{137} Z^{1/3}\frac{m_e c^2}{Pc}. \tag{25}$$

Total elastic scattering cross section for the proton energy of T is calculated by

$$\sigma_{el}(T) = 2\pi \int_{\theta_{cut}}^{\pi} \frac{d\sigma_{el}}{d\Omega}\sin\theta d\theta. \tag{26}$$

Figure 4 shows the calculated total cross section (equation (26)) of proton elastic scattering in water as a function of T. Reproducibility of the nuclear stopping power was confirmed in comparison with ICRU data [37].

5.3.2. Angular distributions. In the early stages of the development of data compilation, angular distributions of elastic scattering calculated by the CMTC were examined. The Monte Carlo full slowing-down tracks showed unrealistic tortuous tracks for energies greater than 10 MeV. Therefore, we adopted an alternative formula called the Mott-scattering formula, effective for high-energy protons [40]:

$$\frac{d\sigma_{el}(\theta)}{d\Omega} = \frac{1}{4} N_A \frac{Z^2}{A} z^2 r_e^2 \left(\frac{m_e c}{P\beta}\right)^2 \frac{1 - \beta^2 \sin^2(\theta/2)}{\sin^4(\theta/2)}, \tag{27}$$

where N_A = the Avogadro constant and A = molar mass of the scattering medium. The Mott formula was derived assuming the repulsive Coulomb force not taking into account the

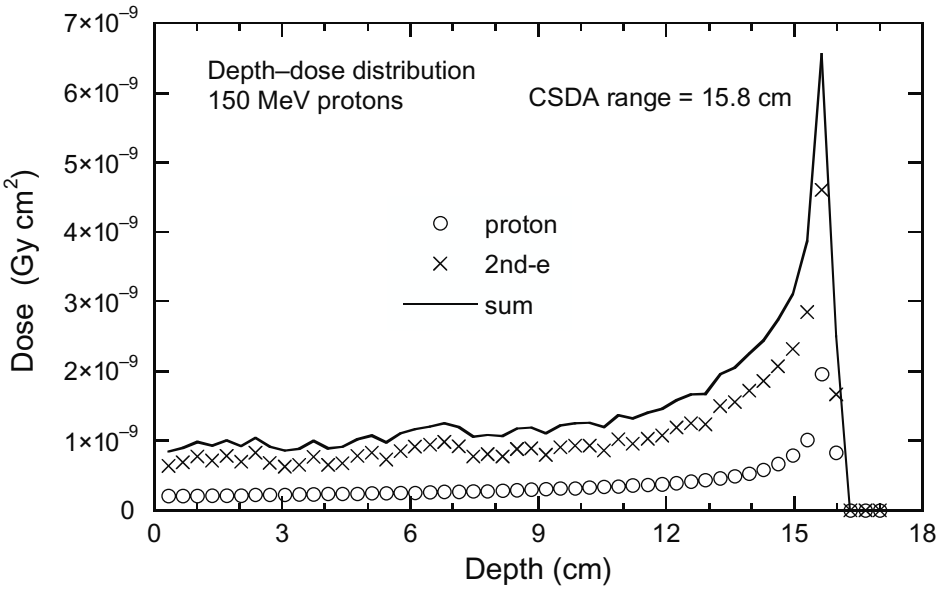

Figure 6. Calculated depth–dose curves for protons and secondary electrons and their sum for a broad parallel beam of protons with 150 MeV. These distributions were obtained from the full slowing down proton tracks.

screening by atomic electrons for the relativistic energy of projectiles. At the non-relativistic limit, this formula is reduced to the classical Rutherford scattering formula. Both formulae provide less-deflective tracks than the CMTC results because the screening effect is neglected.

5.4. Depth–dose distribution

The reliability of cross sections and angular distributions for protons can be tested by several macroscopic quantities such as stopping powers, continuous slowing down approximation (CSDA) ranges and depth–dose distributions. We confirmed that the calculated stopping powers and ranges agree well with the published data for liquid water in the energy range up to 200 MeV [37]. Depth–dose distribution is a severe criterion on the track structure code, because it is affected by not only stopping powers but also proton deflections.

Figure 6 shows the depth–dose curve in water phantom for a broad parallel beam of protons with 150 MeV. Absorbed dose is represented in Gy cm^2 units. In this case, the HEPHIST code was executed under the 'full slowing down' mode. The depth of the Bragg peak is in agreement with the CSDA range of 15.8 cm for liquid water. This supports an adoption of the Mott-scattering formula for angular distributions for high-energy protons. The calculated distribution implies the capability of the microscopic track structure to obtain such a macroscopic quantity in the ∼cm region. The contribution of secondary electrons to the total dose amounts to 70% over the whole depth.

5.5. Radial dose distribution

The radial dose distribution, which is the energy absorbed locally at a certain radial distance from the path of a primary particle, has been used to check the reliability of track structure calculations. Figure 7 shows the radial dose profiles around the path of protons with various energies. According to the definition of radial dose distribution, the energy depositions along the

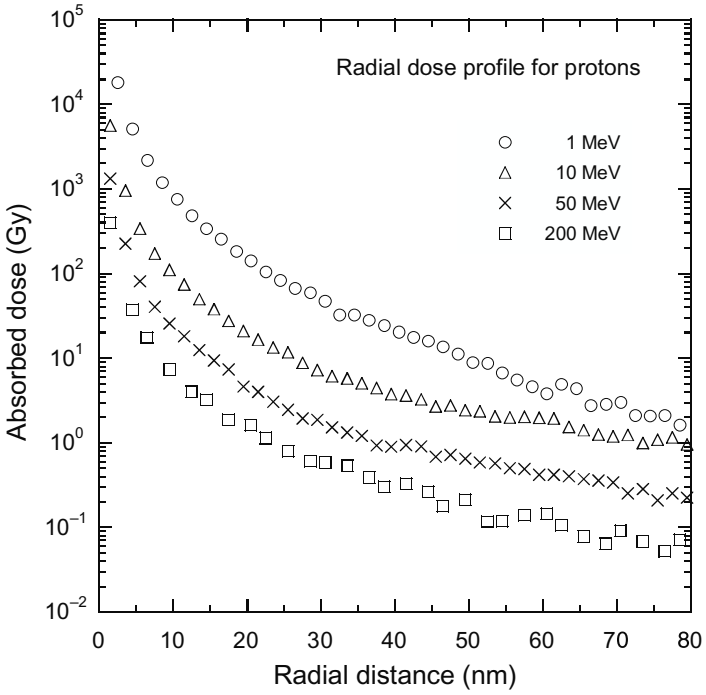

Figure 7. Calculated radial dose profiles at 1, 10, 50 and 200 MeV proton paths.

proton track itself are excluded in dose calculations. Energies deposited only due to secondary electrons were accumulated within a coaxial shell with a radial interval of 1 nm along the proton track with a short length.

5.6. Microdosimetry

A tissue equivalent proportional counter (TEPC) is the principal instrument for measuring the distribution of energy deposited in a specific volume. The instrument is commonly designed as a spherical or a cylindrical volume with varying sensitive volume. The standard representation of a microdosimetric spectrum is the dose distribution $yd(y)$ in the lineal energy y, in which the area between any two values of y indicates the dose delivered in that range. Distributions of lineal energy were simulated for various proton energies through a wall-less counter, 1 μm diameter, using proton tracks generated by the HEPHIST code.

Figure 8 shows a comparison of the calculated spectrum for 50 MeV protons between the present work and the published data by Nikjoo *et al* [41]. The theory of microdosimetry defines several average parameters; the frequency average lineal energy $\overline{y_F}$ and specific energy $\overline{z_F}$, and the dose average $\overline{y_D}$ and $\overline{z_D}$. Table 2 shows such average parameters for various proton energies in comparison with the published data which were obtained using a track segment code PITS [41]. The parameters calculated by the present code showed a good agreement with the PITS data. The reliability of the HEPHIST code was confirmed within the statistical uncertainties.

6. Electron track simulation in liquid water

Electron track simulation in matter depends on the availability of realistic interaction cross sections over the complete slowing down energy spectrum. The interaction of electrons with

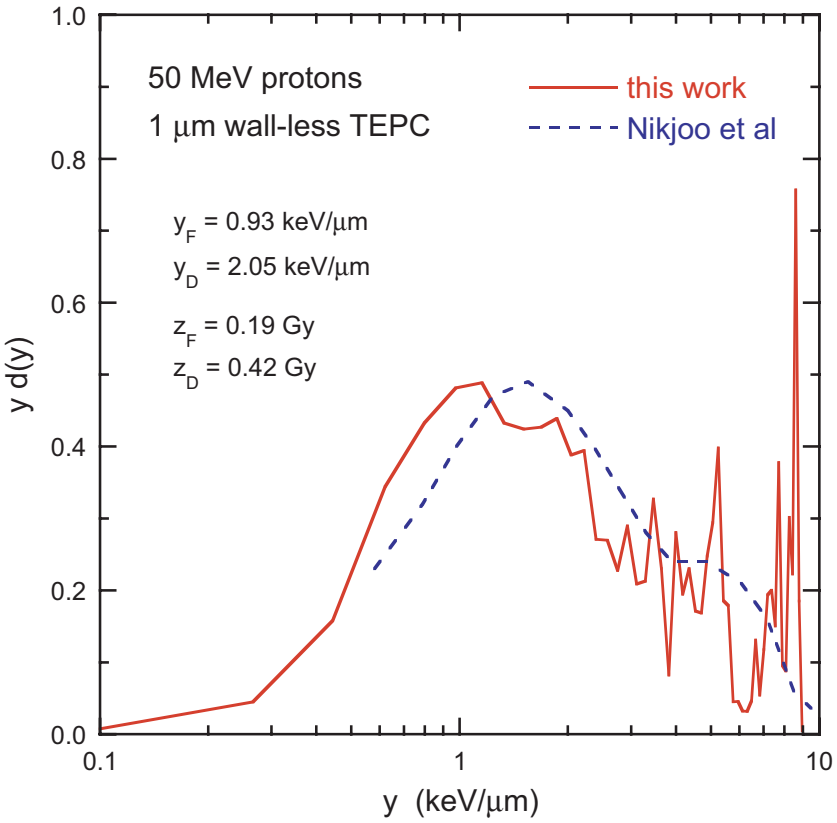

Figure 8. Calculated lineal energy distributions y d(y) of 50 MeV protons in simulated wall-less TEPC for a site diameter of 1 micron.

Table 2. Microdosimetric quantities for a wall-less TEPC with a site diameter of 1 μm calculated using the HEPHIST code.

Proton energy (MeV)	$\overline{y_F}$ (keV μm^{-1})	$\overline{y_D}$ (keV μm^{-1})	$\overline{z_F}$ (Gy)	$\overline{z_D}$ (Gy)
1	25.6	29.5	5.23	6.02
5	6.36	8.09	1.30	1.65
10	3.81	5.15	0.78	1.05
20	2.06	3.28	0.42	0.67
40	1.09	2.08	0.22	0.42
50	0.93	2.05	0.19	0.42
100	0.50	1.32	0.10	0.27
150	0.33	1.05	0.068	0.21
200	0.26	0.74	0.053	0.15

water vapour is relatively well understood and scattering cross sections are generally available to a good accuracy (~10–20%) by either theory or experiment [42]. This is in sharp contrast to the condensed phase (i.e. liquids and solids), where experimental data are scarce and the underlying theory is computationally intractable [43]. Therefore, a large number of codes simulate electron tracks in a unit-density water-vapour medium [44]. However, due to the long-range

polarization-screening effects in the condensed phase, scattering cross sections are expected to differ from those in the gas phase [45].

The most important interaction coefficients for electron track simulation are the differential cross sections (DCSs) for elastic ($d\sigma_{el}/d\Omega$) and inelastic ($d\sigma_{inel}/dE$) scattering which determine, respectively, the scattering angle (Ω) and energy loss (E) in a single collision. The elastic mean free path (EMFP, λ_{el}) and inelastic mean free path (IMFP, λ_{inel}) scattering are then readily obtained from the corresponding DCSs. For use in track simulation studies, the DCSs are most conveniently calculated within the relativistic plane-wave Born-approximation (PWBA) which provides a near-exact framework at sufficiently high projectile energies [46].

6.1. Elastic scattering

For elastic electron scattering by atomic nuclei, the PWBA with a Wentzel-like potential, $V(r) = -(Z/r)e^{-r/R}$, where $R = 0.885\,\alpha_0 Z^{-1/3}$, leads to particular useful analytic forms for both the DCS and EMFP, which are often referred to as the screened Rutherford formulae [47]:

$$\frac{d\sigma_{el}}{d\Omega} = Z^2 r_e^2 \left(\frac{1-\beta^2}{\beta^4}\right) \frac{1}{(1-\cos\theta+2\eta_W)^2}, \tag{28}$$

$$\lambda_{el}^{-1} = \pi Z^2 r_e^2 N \left(\frac{1-\beta^2}{\beta^4}\right) \frac{1}{\eta_W(\eta_W+1)}, \tag{29}$$

where θ is the scattering angle between the emitted and the incident electrons, N is the density of scattering centres, Z the atomic number of the material, r_e the classical electron radius, $\beta(\equiv \upsilon/c)$ the ratio of the incident electron velocity (υ) to the velocity of light (c) and η_W a screening parameter which reduces the cross section at small scattering angles (associated with large impact parameters). Within the Wentzel model η_W takes the form

$$\eta_W = \frac{1.7\times10^{-5}Z^{2/3}}{\tau(\tau+2)}, \tag{30}$$

where $\tau = T/m_0c^2$ (T and m_0 are the electron kinetic energy and rest mass, respectively). Improved values for the screening parameter have been evaluated by Moliere [6]

$$\eta_M = \left[1.13 + 3.76\left(\frac{Z}{137\beta}\right)^2\right]\eta_W \tag{31}$$

and by Nigam *et al* [48]

$$\eta_N = (1.12)^2\eta_W. \tag{32}$$

For electron track simulations in water, it is customary to use empirically derived screening parameters by taking into account relevant experimental data. One such very popular screening parameter is that of Grosswendt and Waibel [49] based on nitrogen data

$$\eta_G = (1.64 - 0.0825\ \ln\ T)\eta_W. \tag{33}$$

A screening parameter specifically derived from water-vapour data is that of Uehara *et al* [31]

$$\eta_U = \begin{cases} 1.198\eta_W, & T < 50\,\text{keV}, \\ \eta_M, & T \geqslant 50\,\text{keV}. \end{cases} \tag{34}$$

A value for the screening parameter between $0.6\eta_W$ and $1\eta_W$ has also been suggested in [50] from an analysis of measurements on various low-Z molecules.

At high energies, the PWBA overestimates the DCS at large scattering angles due to the neglect of relativistic spin effects. A simple scheme has been suggested [50], whereby the DCS is expressed as the product of (28) and the ratio of the Mott to the Rutherford cross section which reads [51]

$$K_{\mathrm{rel}}(\theta) = 1 - \beta^2 \sin^2\frac{\theta}{2} + \pi\beta\frac{Z}{137}\left(1 - \sin\frac{\theta}{2}\right)\sin\frac{\theta}{2}. \tag{35}$$

In many simulation codes the (less-important) angular deflections in inelastic collisions are accounted for in an approximate way by replacing Z^2 by $Z(Z+1)$ in (28) and (29). In [9], an additional suggestion is made to also replace Z by an effective atomic number, Z_{eff}, which, tentatively, equals the corresponding photoelectric value (i.e. $Z_{\mathrm{eff}} \approx 7.4$–$7.5$ for water).

The above discussion neglects condensed phase effects and, therefore, is strictly applicable to electron track simulation in water vapour. A more consistent approach than the PWBA is the relativistic partial wave expansion method (PWEM) [52], where condensed phase effects may be accounted for through an appropriate interaction potential [53]. Unfortunately, calculations by the PWEM are much more cumbersome compared to the PWBA and, importantly, they do not lead to a closed analytic form. The NIST electron elastic-scattering cross-section database (SRD 64) [54] provides PWEM data within the static-exchange approximation (equivalent to the first-order perturbation theory) for electron energies between 50 eV and 300 keV and elements with atomic number (Z) from 1 to 96 using the algorithm of Salvat and Mayol [55]. A detailed discussion of various aspects of these calculations is provided in [56]. A comparison of elastic-DCSs and EMFPs for water vapour is presented in figures 9 and 10, respectively. The NIST values are obtained from a linear combination of the corresponding quantities of the composite atoms, i.e. $\mathrm{d}\sigma_{\mathrm{NIST}}/\mathrm{d}\Omega = 2\mathrm{d}\sigma_{\mathrm{H}}/\mathrm{d}\Omega + \mathrm{d}\sigma_{\mathrm{O}}/\mathrm{d}\Omega$ and $\lambda_{\mathrm{NIST}}^{-1} = 2\lambda_{\mathrm{H}}^{-1} + \lambda_{\mathrm{O}}^{-1}$. They are compared with calculations based on the screened Rutherford formulae (29) and (30) using different screening parameters (31)–(35) as well as the Mott spin-correction (36). With respect to the DCS (figure 9), the agreement at 100 keV is satisfactory at small scattering angles where the DCS is largest. Differences increase with scattering angle, where the use of the Mott spin-correction substantially improves the agreement with NIST. At 100 eV the NIST data are most uncertain due to the neglect of polarization and absorption effects (equivalent to second-order perturbation terms). As expected, the choice of the screening parameter becomes important at low energies and affects the DCS mostly at small scattering angles. The Moliere screening leads to unrealistic DCSs, whereas the magnitude of the Mott spin-correction is negligible. With respect to the EMFP (figure 10), it seems that by an appropriate selection of the screening parameter very good agreement with NIST's more elaborate PWEM may be obtained above a few keV. In the sub-keV region where both the static-exchange approximation (used by NIST) and the assumptions of the PWBA (underlying the screened Rutherford formulae) deteriorate, discrepancies increase.

The use of a solid-state potential in the PWEM is known to reduce the DCS at small scattering angles and electron energies below a few tens of keV [53]. The magnitude of condensed-phase effects on elastic electron scattering in water is not yet clear. For example, the experimental data of Michaud *et al* [43] for very low-energy electrons (<100 eV) suggest that the EMFP in amorphous ice is larger compared to the vapour phase by a factor of 2–10. On the other hand, the recent PWEM calculations of Aouchiche *et al* [57] for gaseous and liquid water reveal a very small phase effect ($\sim$15%) above 100 eV which further diminishes at lower energies.

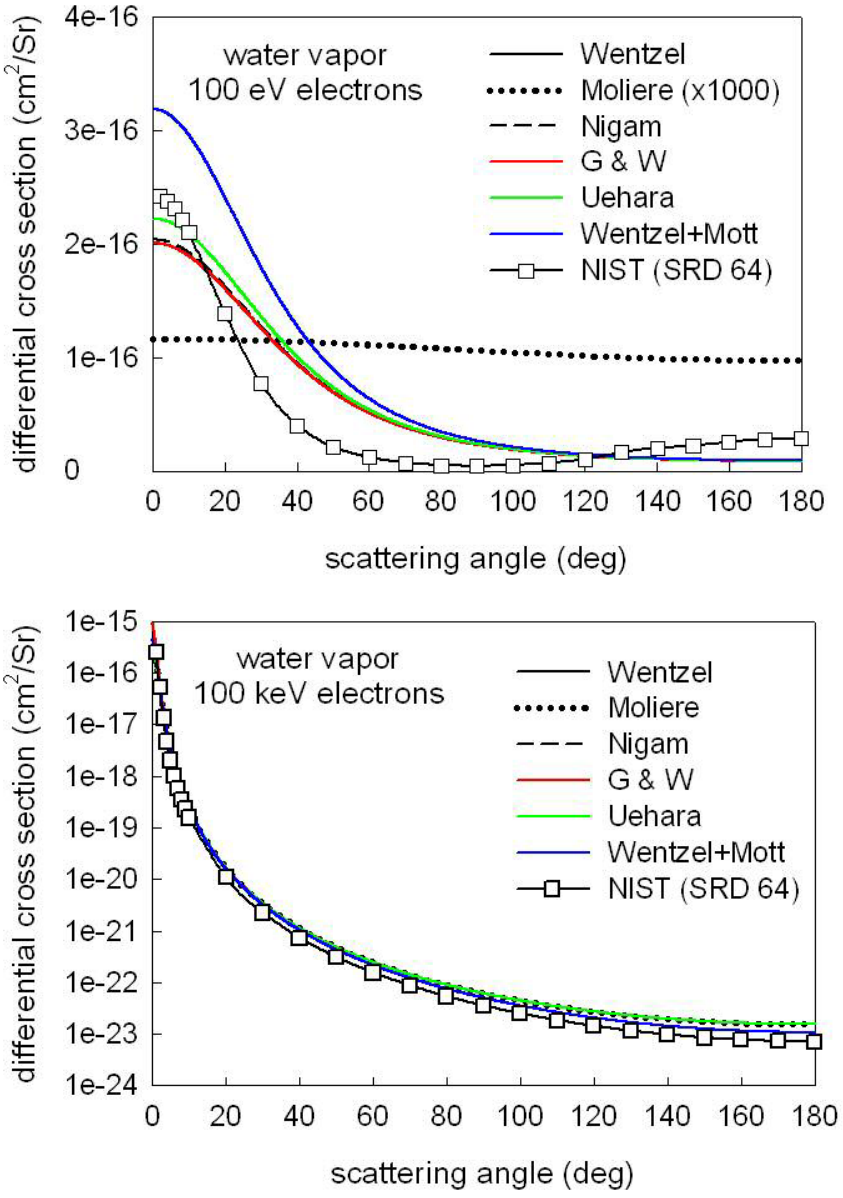

Figure 9. The differential cross section for elastic scattering for (a) 100 eV and (b) 100 keV electrons in water. Comparison of the NIST database SRD 64 [51] with the screened Rutherford formula (1) using the screening parameters of (3)–(7) and the Mott spin-correction (8).

6.2. Inelastic scattering

The main challenge in the study of inelastic electron scattering from atomic electrons is to properly account for binding effects. This is the main reason why binary collision models fail under various circumstances. The PWBA provides a consistent framework for accounting for binding effects through the use of material-specific structure functions. An in-depth discussion of relativistic inelastic electron-scattering in condensed matter within the PWBA has recently been presented by Fernández-Varea *et al* [58]. The inelastic DCS may be expressed as the sum

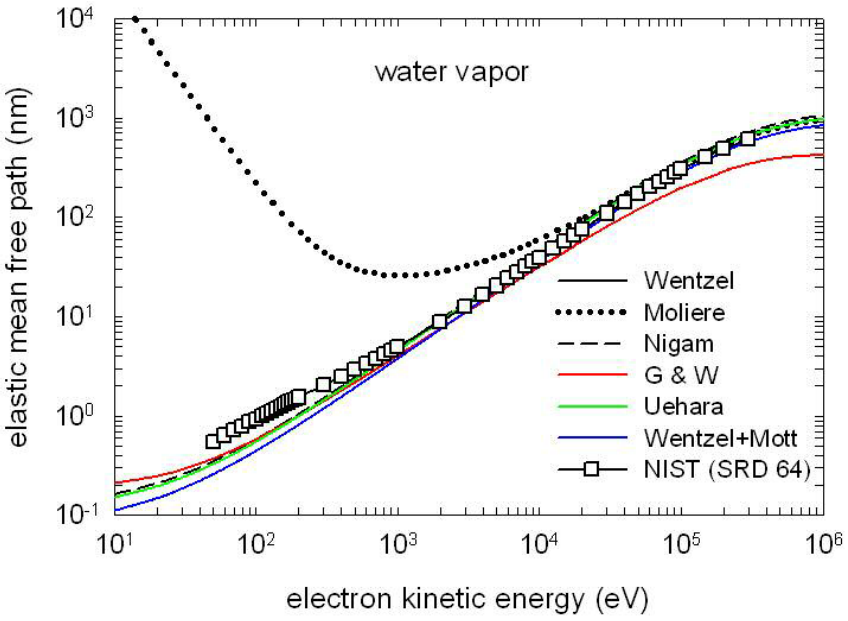

Figure 10. The mean free path for elastic scattering of electrons in water over the 10 eV to 1 MeV energy range. Comparison of the NIST database SRD 64 [54] with the screened Rutherford formula (2) using the screening parameters of (3)–(7) and the Mott spin-correction (8).

of two terms:

$$\frac{\mathrm{d}\sigma_{\mathrm{PWBA}}}{\mathrm{d}E} = \frac{\mathrm{d}\sigma^{(\mathrm{L})}_{\mathrm{PWBA}}}{\mathrm{d}E} + \frac{\mathrm{d}\sigma^{(\mathrm{T})}_{\mathrm{PWBA}}}{\mathrm{d}E}, \tag{36}$$

where the superscripts 'L' and 'T' denote the longitudinal and transverse contributions, respectively. The longitudinal term is obtained from:

$$\frac{\mathrm{d}\sigma^{(L)}_{\mathrm{PWBA}}}{\mathrm{d}E} = \frac{1}{\pi\alpha_0 N mc^2\beta^2}\int_{Q_{\min}}^{Q_{\max}} \frac{1+Q/mc^2}{Q(1+Q/2mc^2)}\,\mathrm{Im}\left[\frac{-1}{\varepsilon(E,q)}\right]\mathrm{d}Q, \tag{37}$$

where E and q are the energy and momentum transfers, respectively, Q is the free-recoil energy defined by $Q(Q+2mc^2) = (cq)^2$ and $\varepsilon(E, Q) = \varepsilon_1(E, Q) + \mathrm{i}\varepsilon_2(E, Q)$ is the complex-value dielectric response function of the material. The $\mathrm{Im}[-1/\varepsilon(E,q)] = \varepsilon_2(E,q)/|\varepsilon(E,q)|^2$ term is the so-called loss function. The limits of integration in (37) are

$$Q_{\max,\min} = \left\{\left[\sqrt{T(T+2mc^2)} \pm \sqrt{(T-E)(T-E+2mc^2)}\right]^2 + (mc^2)^2\right\}^{1/2} - mc^2. \tag{38}$$

The transverse term in (36) is obtained from

$$\frac{\mathrm{d}\sigma^{(\mathrm{T})}_{\mathrm{PWBA}}}{\mathrm{d}E} = \frac{1}{\pi\alpha_0 N\beta^2 mc^2}\,\mathrm{Im}\left[\frac{-1}{\varepsilon(E,q=0)}\right]\left[\ln\left(\frac{1}{1-\beta^2}\right) - \beta^2\right]. \tag{39}$$

Note that the transverse term vanishes at the non-relativistic limit ($\beta \ll 1$) and that only interactions with zero momentum transfer ($q = 0$) contribute to its magnitude [59]. The

connection between condensed and gas phase inelastic cross-sections is obtained from [58]

$$\frac{\mathrm{d}f(E,q)}{\mathrm{d}E} = E(1+Q/mc^2)\frac{1}{8N\pi^2\alpha_0^3R^2}\mathrm{Im}\left[\frac{-1}{\varepsilon(E,q)}\right], \tag{40}$$

where $\mathrm{d}f(E,q)/\mathrm{d}E$ is the generalized oscillator strength. In the gas phase, or for high-energy transfers in the condensed phase $\varepsilon_2(E,q) \ll \varepsilon_1(E,q) \approx 1$ so $\mathrm{Im}[-1/\varepsilon(E,q)] \approx \varepsilon_2(E,q)$.

The main advantage of the PWBA is that, essentially, the inelastic scattering problem is reduced to that of finding an appropriate description of either the atomic/molecular oscillator strength or the solid-state dielectric response function over the complete range of energy- and momentum-transfer (i.e. the so-called Bethe surface). *Ab initio* calculations, due to their complexity, are generally limited to atomic systems [60]. For use in track simulations semi-empirical models based on optical data and momentum-extension schemes have proved to be most suitable [61] and have been widely applied to condensed water [62]–[66]. In particular, the use of experimental optical data automatically accounts for many-body effects (e.g. polarization, correlation, collective excitations) that are still computationally intractable. Perhaps the only limitation is the scarcity of experimental data at finite momentum transfer. The versatility of the extended-optical-data methodology allows the implementation of different dispersion approximations for the momentum-dependence of the dielectric response function. The application of the most popular dispersion schemes, such as those of Lindhard, Mermin, Ritchie, Penn, Ashley and Liljequist to condensed water have been investigated by Emfietzoglou *et al* [67]. In particular, the convenient analytic properties of Ritchie's extended-Drude model have been exploited by Emfietzoglou *et al* [68], who developed an improved dielectric response function for liquid water consistent with the experimental data at both zero and finite momentum transfers. The new model is based on the parametrization of the experimental $\mathrm{Im}(\varepsilon) = \varepsilon_2$ data by a linear combination of Drude-type dielectric functions

$$\varepsilon_2(E,q) = E_\mathrm{p}^2\left[\sum_i^{\mathrm{ioniz}} D_2(E,q;\,f_i,E_i,\gamma_i) + \sum_j^{\mathrm{excit}} \tilde{D}_2(E,q;\,f_j,E_j,\gamma_j)\right], \tag{41}$$

where $E_\mathrm{p} = \hbar(4\pi ne^2/m)^{1/2}$ is the plasma energy ($\sim$21.46 eV for liquid water) and the notation D_2 and $\tilde{D}_2$ stands for the 'normal' and 'derivative' Drude functions

$$D_2(E,q;\,f_i,E_i,\gamma_i) = \frac{f_i(q)\gamma_i(q)E}{((E_i+(q^2/2m)g(q))^2-E^2)^2+(\gamma_i(q)E)^2}, \tag{42a}$$

$$\tilde{D}_2(E,q;\,f_j,E_j,\gamma_j) = \frac{2f_j(q)\gamma_j^3(q)E^3}{((E_j^2-E^2)^2+(\gamma_j(q)E)^2)^2}. \tag{42b}$$

The subscripts i and j denote, respectively, the ionization and excitation channels used in the deconvolution of the experimental spectrum. Appropriate ionization cut-offs and a band-gap energy (as an approximate excitation threshold) are applied to truncate the non-physical extension of the Drude functions to sub-threshold values. The corresponding analytic expressions of the Drude functions used to represent $\mathrm{Re}\,\varepsilon = \varepsilon_1$ (i.e. D_1 and $\tilde{D}_1$) are obtained from the Kramers–Kronig relations. The details of the above procedure and the values of the Drude coefficients along with their q-dependence are given in [68].

Even in the case where an accurate dielectric response function is available, inelastic calculations within the PWBA are known to lead to sizeable errors at sub-keV energies and, in particular, at the region of the maximum. Alternative methodologies, such as, for example, the distorted-wave Born approximation, are notoriously more difficult to use and, therefore, so far have been applied only to a limited number of atomic systems [60]. However, it has been recognized that for track simulations, PWBA calculations may be safely extended down to low electron energies if supplemented with simple correction terms that account in an approximate way for exchange and higher order perturbation effects [69]. The former may be conveniently accounted for by either the Ochkur approximation or by the use of Mott-like Born terms whereas the latter by either a simple Coulomb-field velocity transformation (similar to the 'Burgess' denominator in the binary-encounter approximation) or a second-order perturbation term analogous to the Barkas Z^3-term in the stopping of heavy charged particles. The effect of various model approximations within the extended-optical-data methodology has been investigated in [70]. The following scheme has been found to effectively incorporate Born corrections (BC) in the DCS of low-energy electrons (<10 keV) [71]:

$$\frac{\mathrm{d}\sigma_{\mathrm{BC}}}{\mathrm{d}E} = \frac{\mathrm{d}\sigma_{\mathrm{PWBA}}}{\mathrm{d}E} + \frac{\mathrm{d}\sigma_{\mathrm{2nd}}}{\mathrm{d}E} + \frac{\mathrm{d}\sigma_{\mathrm{ex}}}{\mathrm{d}E}, \tag{43}$$

where

$$\frac{\mathrm{d}\sigma_{\mathrm{2nd}}}{\mathrm{d}E} = -\frac{2}{\pi\alpha_o TN} L(E;\xi)\,\mathrm{Im}\left[\frac{-1}{\varepsilon(E, q=0)}\right], \tag{44}$$

$$\frac{\mathrm{d}\sigma_{\mathrm{ex}}(E,T)}{\mathrm{d}E} = \sum_{i}^{\mathrm{ioniz.}} \left\{ \frac{\mathrm{d}\sigma_i(T-E+B_i,T)}{\mathrm{d}E} - \left[\frac{\mathrm{d}\sigma_i(E,T)}{\mathrm{d}E} \times \frac{\mathrm{d}\sigma_i(T-E+B_i,T)}{\mathrm{d}E}\right]^{1/2} \right\}. \tag{45}$$

The function $L(E;\xi)$ in (17) depends on the parameter ξ associated with the cut-off distance of soft ($q=0$) collisions [72] whereas in the right-hand side of (18) σ_i denotes the sum $\sigma^{(i)}_{\mathrm{PWBA}} + \sigma^{(i)}_{\mathrm{2nd}}$. In figure 11 the inverse-IMFP (i.e. macroscopic inelastic cross section) of electrons in liquid water is presented over the 10 eV–1 MeV energy range. Relativistic corrections become important above a few tens of keV with the main contribution coming from the kinematics, since the transverse term contributes little ($<10\%$) up to 1 MeV. The BC terms are progressively important below 1 keV. In figure 12, the IMFP of electrons in liquid water is presented over the 10 eV–10 keV energy range. The PWBA results with and without BCs are compared with those obtained from the TPP-2M formula of NIST [73]. The differences from the NIST values increase with decreasing electron energy and are generally between 20 and 40% over the 10 keV to 100 eV range. The effect of BCs upon the IMFP remains small (up to 10%) down to 300 eV; it increases drastically though at lower energies reaching $\sim$50% at 100 eV.

Radial distributions of absorbed energy in the vapour and liquid phases of water (both at unit density) calculated from track simulations are presented in figure 13 for point-isotropic monoenergetic electron sources of 0.1, 1 and 10 keV. The energy deposited (average over 10^5 tracks) is scored in concentric spherical shells of thickness 0.5 nm. For both phases, we use the same set of elastic cross sections calculated from the screened Rutherford formulae. The inelastic cross sections for the vapour have been described in [74], whereas those of the liquid are based on the dielectric response function presented in [68]. The electron cut-off energy for both the primary and all the subsequent generations of electrons was set at 1 Ry. It is evident

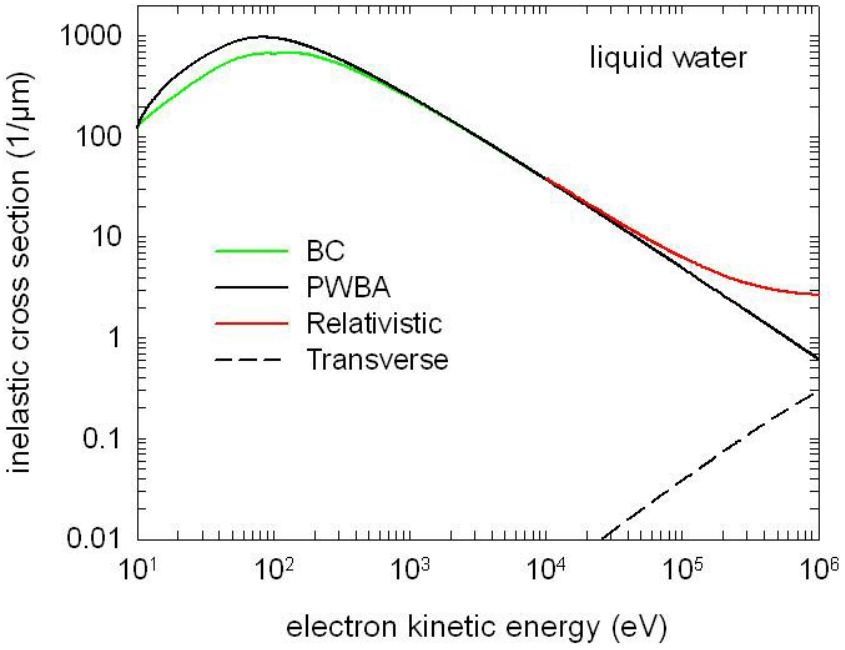

Figure 11. The inelastic scattering cross section (or inverse inelastic mean free path) of electrons in liquid water over the 10 eV to 1 MeV energy range. The dielectric response function (14) and (15) of [68] has been used as an input.

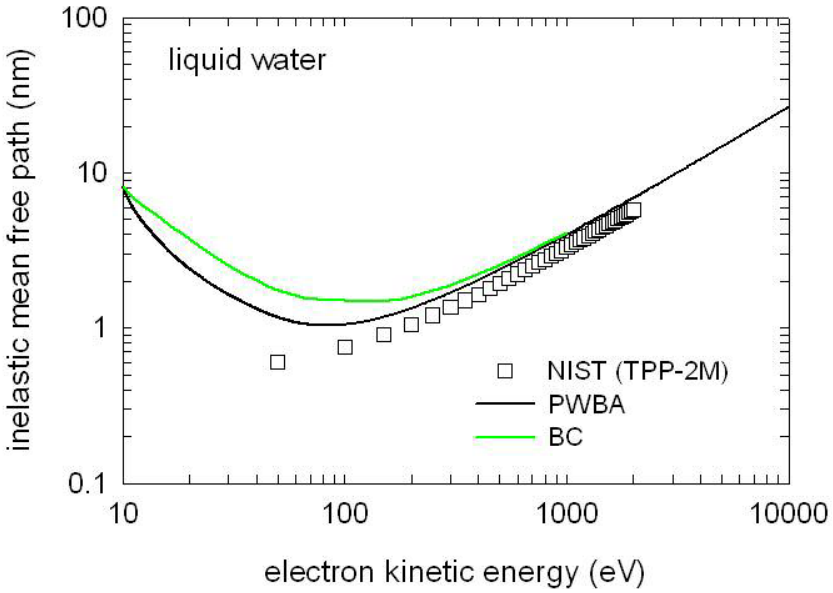

Figure 12. The inelastic mean free path of electrons in liquid water over the 10 eV to 10 keV energy range. The results from the TPP-2M formula of NIST [73] are compared with those obtained from the PWBA with and without BC. The dielectric response function (14) and (15) of [68] was used in the PWBA and BC calculations.

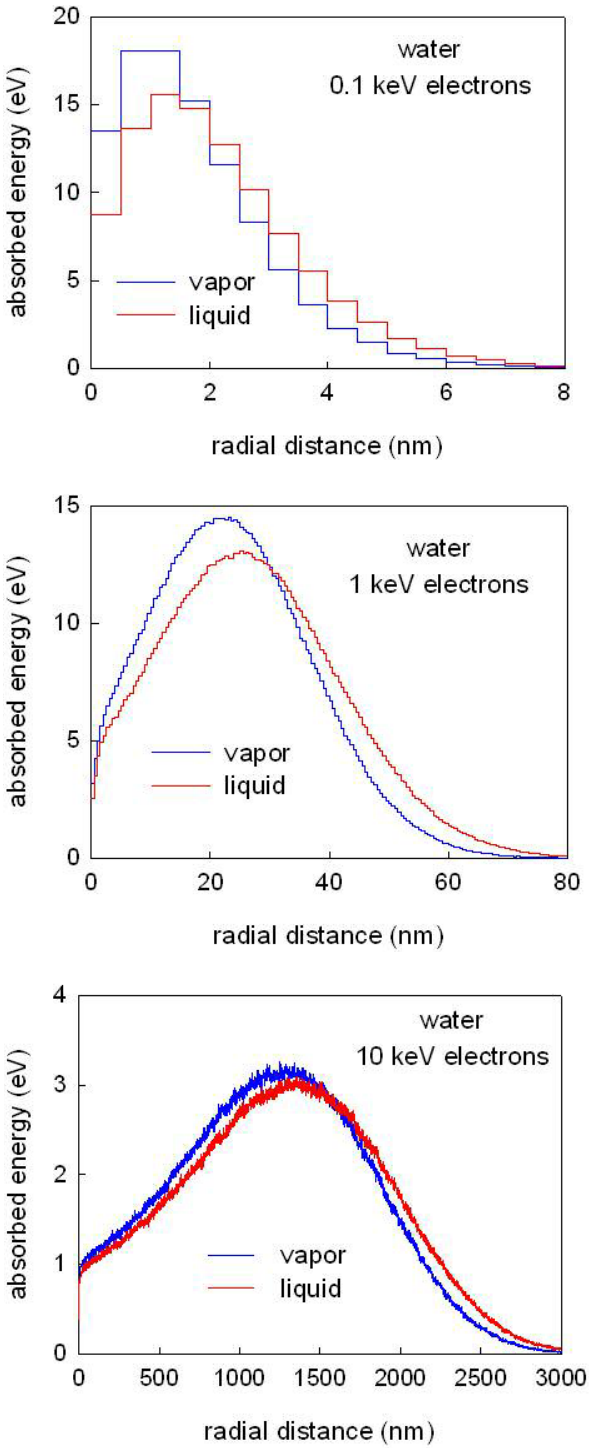

Figure 13. Comparison of radial distribution of energy deposition for (a) 0.1, (b) 1 and (c) 10 keV electrons in the vapour and liquid phases of water (both at unit densities).

that polarization and screening effects in the liquid phase, as reflected in its dielectric response function, result in a higher electron penetration and a more diffuse energy-deposition pattern. The effect is more pronounced as the electron energy decreases where cross section differences between the two phases become largest [75].

7. Conclusions

This paper has presented a brief discussion on biological and therapeutic efficacies of heavy ions with low atomic number (z). Biophysical aspects of radiation tracks are best explored with the context of microdosimetry as seen in figures 1 and 8. The paper argues that the use of heavy ions such as lithium and carbon will bring much desired improvement in radiation therapy. The paper has presented the first example of a full event by event Monte Carlo track structure generating the full slowing down track of a typical radiotherapy proton beam. The new tool will bring the ability to examine in much more detail the biophysical features of the proton track in the Bragg peak region. And lastly, the paper presented cross sections for electron track simulations in liquid water. The electron cross sections in liquid water were calculated using the new dielectric model of low-energy electrons, which is accurate to better than ∼10% down to 100 eV. On Earth, all radiobiological experiments and calculations are compared against the gold standard data for x-rays and gamma photons. Similarly, in space and in radiation therapy with heavy ions all data need to be compared with protons as the gold standard. It is for this reason that good and reliable proton data need to be established.

References

[1] Nikjoo H and Uehara S 2004 *Charged Particle and Photon Interactions with Matter: Chemical, Physiochemical, and Biological Consequences with Applications* ed A Mozuumder and Y Hatano (New York: Marcel Dekker)
[2] Nikjoo H and Khvostunov I K 2003 *Int. J. Radiat. Biol.* **79** 43
[3] Nikjoo H and Khvostunov I K 2006 *Int. J. Low Radiat.* **3** 143
[4] Nikjoo H, O'Neill P, Wilson W E and Goodhead D T 2001 *Radiat. Res.* **156** 577
[5] Nikjoo H, O'Neill P, Goodhead D T and Terrissol M 1997 *Int. J. Radiat. Biol.* **71** 467
[6] Charlton D E, Nikjoo H and Humm J L 1989 *Int. J. Radiat. Biol.* **56** 1
[7] Prise K M *et al* 1998 *Int. J. Radiat. Biol.* **74** 173
[8] Frankenberg D, Brede H J, Schrewe U J, Steinmetz C, Frankenberg-Schwager M, Kasten G and Pralle E 2000 *Adv. Space Res.* **25** 2085
[9] Rydberg B, Cooper B, Cooper P K, Holley W R and Chatterjee A 2005 *Radiat. Res.* **163** 526
[10] Ottolenghi A, Ballarini F and Merzagora M 1999 *Radiat. Environ. Biophys.* **38** 1
[11] Campa A *et al* 2005 *Int. J. Radiat. Biol.* **81** 841
[12] Hsiao Y and Stewart R D 2008 *Phys. Med. Biol.* **53** 233–44
[13] Harrison L, Hatahet Z and Wallace S S 1999 *J. Mol. Biol.* **290** 667
[14] David-Cordonnier M H, Cunniffe S M, Hickson I D and O'Neill P 2002 *Biochemistry* **41** 634
[15] Sutherland B M, Bennett P V, Sidorkina O and Laval J 2000 *Proc. Natl Acad. Sci. USA* **97** 103
[16] Chaudhry M A and Weinfeld M 1997 *J. Biol. Chem.* **272** 15650
[17] Nikjoo H, Goodhead D T, Charlton D E and Paretzke H G 1994 Energy deposition by monoenergetic electrons in cylindrical targets *MRC Monograph 1994* MRC Radiobiology Unit, Harwell, UK
[18] Nikjoo H, Goodhead D T and Charlton D E 1988 Energy deposition in cylindrical volumes in water irradiated with ultrasoft x-rays of energy 0.28, 1.5, 4.5 and 8.1 keV *MRC Radiobiology Unit Monograph 88* MRC Radiobiology Unit, Harwell, UK

[19] Nikjoo H, Boyden-Pratt N, Uehara S and Goodhead D T 2001 Energy deposition by monoenergetic protons in cylindrical targets *MRC Monograph 2001* MRC Radiation and Genome Stability Unit, Harwell, UK
[20] Charlton D E, Goodhead D T, Wilson W E and Paretzke H G 1985 Energy deposition by monoenergetic protons and alpha-particles in cylindrical targets *MRC Monograph 1985* MRC Radiobiology Unit, Harwell, UK
[21] Nikjoo H, Boyden-Pratt N, Girard P, Uehara S and Goodhead D T 2002 Energy deposition by alpha-particles in cylindrical targets *MRC Monograph 2002* MRC Radiation and Genome Stability Unit, Harwell, UK
[22] Kylonen J E, Girard P, Uehara S, Lindborg L and Nikjoo H 2003 Energy deposition by heavy ions in cylindrical targets *MRC Monograph 2003* MRC Radiation and Genome Stability Unit, Harwell, UK
[23] Grindborg J-E, Lillhök J E, Lindborg L, Gudowska I, Söderberg J, Alm Carlsson G and Nikjoo H 2007 *Radiat. Prot. Dosim.* **126** 463–6
[24] Brahme A 2004 *Int. J. Rad. Oncol. Biol. Phys.* **58** 603
[25] Kempe J, Gudowska I and Brahme A 2007 *Med. Phys.* **34** 183
[26] Zelefsky M 2007 private communication, Memorial Sloan Kettering Cancer Center, New York, NY, USA
[27] Slater J, Rossi C, Yonemoto L, Bush D, Jabola B, Levy R, Grove R, Preston W and Slater J 2004 *Int. J. Radiat. Oncol. Biol. Phys.* **59** 348–52
[28] Tsujii H 2007 private communication, National Institute for Radiological Sciences, Chiba, Japan
[29] Svensson H, Ringborg U, Näslund J and Brahme A 2004 *Radiother. Oncol.* **73** 206
[30] Nakamura Y 2004 *Cancer Sci.* **95** 7
[31] Uehara S, Toburen L H and Nikjoo H 2001 *Int. J. Radiat. Biol.* **77** 139
[32] Uehara S, Nikjoo H and Goodhead D T 1993 *Phys. Med. Biol.* **38** 1841
[33] Seltzer S M 1988 *Transport of Electrons and Photons* ed T M Jenkins, W R Nelson and A Rindi (New York: Plenum)
[34] ICRU 1996 Secondary electron spectra from charged particle interactions *ICRU Report* 55
[35] Wilson W E, Miller J H, Toburen L H and Manson S T 1984 *J. Chem. Phys.* **80** 5631
[36] Miller J H and Green A E S 1973 *Radiat. Res.* **54** 343
[37] ICRU 1993 Stopping powers and ranges for protons and alpha particles *ICRU Report* 49
[38] Everhart E, Stone G and Carbone R J 1955 Phys. *Rev.* **99** 1287
[39] Wilson W D and Haggmark L G 1977 Calculations of nuclear stopping, ranges, and straggling in the low-energy region *Phys. Rev.* B **15** 2458
[40] ICRU 1978 Basic aspects of high energy particle interactions and radiation dosimetry *ICRU Report* 28
[41] Nikjoo H, Uehara S, Pinsky L and Cucinotta F A 2007 *Radiat. Prot. Dosim.* **126** 512
[42] Itikawa Y and Mason N 2005 *J. Phys. Chem. Ref. Data* **34** 1
[43] Michaud M, Wen A and Sanche L 2003 *Radiat. Res.* **159** 3
[44] Nikjoo H, Uehara S, Emfietzoglou D and Cucinotta F A 2006 *Radiat. Meas.* **41** 1052
[45] Inokuti M 1991 *Radiat. Eff. Defects Solids* **117** 143
[46] Inokuti M 1971 *Rev. Mod. Phys.* **43** 297
[47] Fernandez-Varea J M, Mayol R, Baro J and Salvat F 1993 *Nucl. Instrum. Methods* B **73** 447
[48] Nigam B P, Sundaresan M K and Wu T-Y 1959 *Phys. Rev.* **115** 491
[49] Grosswendt B and Waibel E 1978 *Nucl. Instrum. Methods* **155** 145
[50] Berger M J, Seltzer S M and Maeda K 1970 *J. Atmos. Terr. Phys.* **32** 1015
[51] Yalcin S, Gurler O, Gultekin A and Gundoglu O 2006 *Phys. Lett.* A **356** 138
[52] Walker D W 1971 *Adv. Phys.* **20** 257
[53] Fernandez-Varea J M, Llovet X and Salvat F 2005 *Surf. Interface Anal.* **37** 824
[54] Powell C J, Jablonski A and Salvat F 2005 *Surf. Interface Anal.* **37** 1068
[55] Salvat F and Mayol R 1993 *Comput. Phys. Commun.* **74** 358
[56] Jablonski A, Salvat F and Powell C J 2004 *J. Phys. Chem. Ref. Data* **33** 409
[57] Aouchiche H, Champion C and Oubaziz D 2008 *Radiat. Phys. Chem.* **77** 107
[58] Fernandez-Varea J M, Salvat F, Dingfelder M and Liljequist D 2005 *Nucl. Instrum. Methods* B **229** 187

[59] Soh D S, Cho B H and Kim Y-K 1982 *Phys. Rev.* A **26** 1357
[60] Segui S, Dingfelder M, Fernandez-Varea J M and Salvat F 2002 *J. Phys. B: At. Mol. Opt. Phys.* **35** 33
[61] Powell C J and Jablonski A 1999 *J. Phys. Chem. Ref. Data* **28** 19
[62] Dingfelder M, Hantke D, Inokuti M and Paretzke H G 1998 *Radiat. Phys. Chem.* **53** 1
[63] Pimblott S M and Siebbeles D A 2002 *Nucl. Instrum. Methods* B **194** 237
[64] Emfietzoglou D 2003 *Radiat. Phys. Chem.* **66** 373
[65] Tan Z, Xia Y, Liu X, Zhao M, Ji Y, Li F and Huang B 2004 *Radiat. Environ. Biophys.* **43** 173–82
[66] Tung C J, Chan W T, Chao T C, Tu Y H and Kwei C M 2007 *Nucl. Instrum. Methods* A **580** 598
[67] Emfietzoglou D, Abril I, Garcia-Molina R, Petsalakis I D, Nikjoo H, Kyriakou I and Pathak A 2008 *Nucl. Instrum. Methods* B **266** 1154–61
[68] Emfietzoglou D, Cucinotta F A and Nikjoo H 2005 *Radiat. Res.* **164** 202
[69] Fernandez-Varea J M 1998 *Radiat. Phys. Chem.* **53** 235
[70] Emfietzoglou D and Nikjoo H 2005 *Radiat. Res.* **163** 98
[71] Emfietzoglou D and Nikjoo H 2007 *Radiat. Res.* **167** 110
[72] Ashley J C 1991 *J. Phys.: Condens. Matter* **3** 2741
[73] Tanuma S, Powell C J and Penn D R 1993 *Surf. Interface Anal.* **21** 165
[74] Emfietzoglou D, Papamichael G, Kostarelos K and Moscovitch M 2000 *Phys. Med. Biol.* **45** 3171
[75] Uehara S, Nikjoo H and Goodhead D T 1999 *Radiat. Res.* **152** 202